This is the peer-reviewed, final accepted version for American Mineralogist, published by the Mineralogical Society of America.
The published version is subject to change. Cite as Authors (Year) Title. American Mineralogist, in press.
DOI: https://doi.org/10.2138/am-2022-8372. http://www.minsocam.org/

Revision 2 Word Count : 5843

Raman shifts of *c*-BN as an ideal P-T sensor for studying water-rock interactions in a diamond anvil cell

Lu'an Ren[1,2], Chao Wang[1,3], Xiaowei Li[2], Renbiao Tao[1,]*

[1.] *Center for High Pressure Science and Technology Advanced Research (HPSTAR), Beijing 100094, China*

[2.] *School of Earth Science and Resources, China University of Geosciences, Beijing 100083, China*

[3.] *School of Earth and Space Sciences, Peking University, Beijing 100871, China*

* Corresponding author: renbiao.tao@hpstar.ac.cn

ABSTRACT

Cubic boron nitride (*c*-BN) has the same structure as diamond. Thus, it shows very inert reaction activity in different chemical environments, even under high-pressure (P) and high-temperature (T) conditions. Furthermore, the P and T-dependent Raman shift of *c*-BN (e.g., TO mode) can be distinguished from that of the diamond anvil (*c*-BN at ~ 1054 cm^{-1} v.s. diamond at ~ 1331 cm^{-1} at ambient conditions), making *c*-BN a potential P-T sensor for diamond anvil cell (DAC) experiments. However, the Raman shift of *c*-BN has not been well studied at high P-T conditions, especially at temperatures above 700 K. In this study, we systematically calibrated the Raman shift of the TO mode (ν_{TO}) for synthetic *c*-BN grains at high-P and high-T conditions up to 15 GPa and 1300 K. Both

ruby (Mao et al. 1986) and Sm^{2+}:SrB_4O_7 (Datchi et al. 2007) were used as internally consistent standards for calibration of *c*-BN P-T sensor. Experimental results showed that Raman shift of *c*-BN is negatively correlated with temperature ($\frac{\partial \nu_{TO}}{\partial T} = -0.02206(71)$), but positively correlated with pressure ($\frac{\partial \nu_{TO}}{\partial P} = 3.35(2)$). More importantly, we found that the P-T cross derivative for Raman shift of *c*-BN ($\frac{\partial^2 \nu_{TO}}{\partial P\, \partial T} = 0.00105(7)$) cannot be ignored, as it was assumed in previous studies. Finally, we calibrated a Raman shift P-T sensor of *c*-BN up to 15 GPa and 1300 K as follows: $P = \frac{A(T)-\sqrt{A(T)^2+0.2194B(T,\Delta\nu)}}{0.1097}$, here $A(T)=3.47(6) + 0.00105(7)T$, $B(T, \Delta\nu_{TO})=2.81(51) - 0.0053(16)T - 1.78(11)\times10^{-5} T^2 - \Delta\nu_{TO}$. The *c*-BN Raman shift P-T sensor in this study fills the P-T gap ranging from previously performed externally resistance-heated to laser-heated DAC experiments. The effect of *c*-BN grain size and Raman system laser power on the calibration were also tested for the P-T sensor. In addition, we conducted three sets of high P-T experiments to test the practicability of *c*-BN P-T sensor for the water-rock interaction experiments in DAC. Testing experiments showed *c*-BN has very stable chemical activity in water and clear Raman signal at high P-T conditions in comparison with other P-T sensors (e.g., ruby, Sm^{2+}:SrB_4O_7, and quartz). In summary, we concluded that the Raman shift of *c*-BN is an ideal P-T sensor for studying water-rock interaction in a DAC, especially at high-P and high-T conditions relevant to subduction zones.

Keywords: Cubic boron nitride (*c*-BN); Raman shift; high P-T sensor; diamond anvil cell; water-rock interactions

1. INTRODUCTION

Monitoring, recording, and reproducing the extensive thermodynamic variables such as pressure and temperature is crucial for all kinds of high-P and high-T experiments, particularly for in-situ diamond anvil cell (DAC) experiments (Mao et al. 1986; Datchi et al. 2007). Dynamic shock compression measurements of materials could provide a primary pressure scale, i.e., an equation of state (EoS) where the density is a function of absolute pressure determined independently from a secondary standard. For instance, the accuracy determinations of the molar volumes of metals (e.g., Au, Ag, or Cu) by X-ray diffraction (XRD) can give precision to the corresponding pressure measurements (Mao et al.1986; Datchi et al.1997; Fei et al., 2007; Trots et al.2013). However, to use these EoS pressure scales, the shock Hugoniot data must be reduced to an isothermal EoS, which can reduce the accuracy of the pressure scale (Goncharov et al.2007). On the other hand, in-situ XRD patterns for EoS have to be collected from a synchrotron radiation station, which dramatically limits the use of the EoS P-T sensor for DAC experiments in a routine laboratory.

In a routine laboratory, pressure in a DAC is normally monitored by a fluorescence shift P-T sensor (e.g., ruby, Sm^{2+}:SrB_4O_7, Sm^{2+}:YAG) in previous works (Barnett et al.

1973; Mao et al. 1986; Hess and Schiferl. 1989; Datchi et al. 1997; Trots et al. 2013). Ruby, Cr^{3+}-bearing α-Al_2O_3, has been widely used as the pressure sensor for DAC experiments in past half a century (Barnett et al. 1973; Piermarini et al 1975; Mao et al. 1978; Mao et al. 1986; Datchi et al. 2007). Recently, Shen et al. (2021) re-calibrated the fluorescence shift of the ruby from the well-calibrated melting line of mercury and found ruby pressure sensor has a very high precision of less than ± 0.2 MPa at room temperature. Sm^{2+}:SrB_4O_7, strontium borate doped with divalent samarium, is proposed as a better fluorescence pressure sensor to substitute ruby at high temperature (Lacam and Chateau. 1989; Datchi et al. 1997; Goncharov et al. 2005; Datchi et al. 2007; Raju et al. 2011; Jing et al. 2013; Rashchenko et al. 2015). The sharp and narrow $^5D_0 - {}^7F_0$ fluorescence line (hereafter 0–0 line) of Sm^{2+}:SrB_4O_7 is more intense than the ruby R1 line. More importantly, the 0–0 line of Sm^{2+}:SrB_4O_7 presenting a significant advantage over ruby is a very small temperature response (Jing et al. 2013). Previous studies suggested that Sm^{2+}:SrB_4O_7 is a very good pressure sensor which allowed us to consider it as "the best fluorescence sensor" for in-situ high-T and high-P experiments in DAC (Datchi et al. 2007; Rashchenko et al. 2015). Similarly, the fluorescence spectrum of Sm^{2+}:YAG was also proposed as an alternative pressure sensor. The Sm^{2+}:YAG is characterized by Y1 and Y2 lines in the main doublet, whose position is almost insensitive to temperature (Hess and Schiferl. 1989). Besides, the Sm^{2+}: YAG is the only

78 fluorescence pressure sensor that was calibrated against "absolute pressure", which was
79 obtained by integrating the bulk modulus determined via Brillouin spectroscopy
80 concerning volumes measured simultaneously by X-ray diffraction (Trots et al. 2013).
81 Another family of compounds, Sm^{2+}:M^{2+}FCl with M representing Ba^{2+} or Sr^{2+}, was also
82 considered as potential pressure sensor because their fluorescence spectra present a single
83 and sharp line with very sensitive pressure shift (1.10 nm/GPa, nearly three times as large
84 as that of the R1 line of the ruby), and relatively small temperature coefficient (Shen et al.
85 1991). Unfortunately, the quenching of the luminescence, due to the increased coupling
86 of the 5*d* and 4*f* electronic states of Sm^{2+}, limits the use of Sm^{2+}:M^{2+}FCl compounds to
87 pressures below 20 GPa (Datchi et al. 1997). In most cases, the ruby and Sm^{2+}-doped P-T
88 sensor material (e.g., Sm^{2+}:SrB_4O_7, Sm^{2+}:YAG, and Sm^{2+}:M^{2+}FCl) have high solubility in
89 aqueous fluids at high-T and high-P conditions, which will result in contamination of
90 water-bearing experimental system in DAC (Datchi et al. 2000; Tropper and Manning
91 2007; Andreani et al. 2013). On the other hand, the easy broadening of the fluorescence
92 peaks at high temperatures significantly reduces the accuracy of pressure measurement
93 using these P-T sensors for experiments performed in the DAC (see R1 and R2 peaks for
94 ruby in Fig. S1; Ragan et al. 1992; Goncharov et al. 2005; Datchi et al. 2007; Trots et al.
95 2013) and the strong fluorescence effect of these sensors at high temperature could cover
96 the Raman signal of small samples in DAC as well. Furthermore, the applicable

97 temperature range of most fluorescence P-T sensors is less than 900 K. Until now, there is
98 still no suitable P-T sensor to bridge the P-T gap ranging from externally resistance-
99 heated DAC (< 900 K) to laser-heated DAC experiments (> 1500 K).

100 The Raman vibration of materials could effectively reflect their structure
101 information at different P-T conditions. Temperature can significantly increase the
102 molecular movement, bond length, and interaction, which can be reflected in the Raman
103 frequency shift. On the other hand, pressure also affects the Raman shift because the
104 pressure-induced reduction of atomic space will change the material structure. Therefore,
105 the Raman shift of materials such as ^{12}C diamond, quartz, carbonates, or zircon could also
106 be calibrated as a P-T sensor for high P-T experiments. Raman shift of culet face of the
107 diamond anvils (^{12}C diamond) has been proposed as a P-T sensor for DAC experiments
108 (Tardieu et al.1990; Datchi et al. 2007; Ono et al. 2014), however, it is only suitable for
109 high-pressure conditions (> 15 GPa) due to its limited sensitivity of determining pressure
110 in the low-pressure range (Datchi et al. 2007). Raman shifts of common minerals (e.g.,
111 carbonates, quartz, zircon) is a function of pressure and temperature, which can be also
112 calibrated as a P-T sensor (Schmidt and Ziemann. 2000; Schmidt and Ziemann. 2013;
113 Farsang et al. 2018; Cui et al. 2020; Farsang et al. 2021). For example, Schmidt and
114 Ziemann (2000) calibrated quartz Raman shift as a sensor at pressure and temperature
115 conditions up to 2.1 GPa and 800 ℃. Facq et al. (2014, 2016) and Farsang et al. (2018)

116 established pressure sensors of different carbonate minerals using *P*- and *T*-induced
117 Raman shifts. Recently, Farsang et al. (2021) re-calibrated Raman shift P-T sensors for
118 most of the carbonates at pressure and temperature conditions up to 6 GPa and 500 °C.
119 Cui et al. (2020) calibrated the zircon Raman shift P-T sensor at pressure and temperature
120 up to 10 GPa and 1000 °C. There are many other minerals that can be used to determine
121 experimental pressure based on their Raman shifts, however, most common minerals
122 could easily dissolve in water and change the experimental system as well at high
123 temperature, which limits their implication as P-T sensor for water-rock interaction
124 experiments in DAC at high P-T conditions.

125 The zinc-blende structure of cubic boron nitride (*c*-BN) is a face-centered-cubic
126 lattice with space group *F*-43*m* (Ono et al. 2015), which has the same structure as
127 diamond. Thus, *c*-BN also shows many excellent physio-chemical properties, such as
128 inert chemical activity, good thermal stability, a wide bandgap, and low dielectric
129 constant (Albe et al. 1997; Datchi and Canny 2004). The *c*-BN Raman spectrum exhibits
130 two intense lines at 1054 cm^{-1} and 1305 cm^{-1} under ambient conditions, corresponding to
131 the Brillouin zone center transverse optical (TO) and longitudinal optical (LO) modes,
132 respectively (Datchi and Canny 2004). The Raman peak of LO mode is normally
133 overlapped with that of the diamond anvils at high P-T conditions (1305 cm^{-1} for LO
134 mode of *c*-BN vs. 1331 cm^{-1} for the diamond at the ambient condition). However, the P-T

dependent TO mode Raman shift of *c*-BN can be distinguished from that of the diamond anvil at ambient conditions (e.g., 1054 cm^{-1} for TO mode of *c*-BN vs. 1331 cm^{-1} for diamond), even at high-P and high-T conditions (Datchi and Canny 2004). Both the inert chemical activity of *c*-BN and distinguishable TO mode Raman signal from the diamond anvil make *c*-BN a potential P-T sensor for DAC experiments, especially for studying the water-rock interaction at high-P and high-T conditions relevant to subduction zones.

The first *c*-BN was synthesized from hexagonal boron nitride (*h*-BN) at 6 GPa and 1400 ℃ by using magnesium metal (Mg) as a catalyst (Wentorf, R.H. 1957). Natural *c*-BN has also been discovered in coesite-bearing chromium-rich ultra-mafic rocks in Tibet, which was believed to have formed in the highly reduced deep mantle (Dobrzhinetskaya et al. 2009). Previous studies have reported the Raman frequency shift of *c*-BN with pressure up to 34 GPa at room temperature (Sanjurjo et al. 1983; Aleksandrov et al. 1989) and with temperature up to 1840 K at room pressure (Alvarenga et al. 1992; Herchen and Capelli. 1993), respectively. Although Datchi and Canny (2004) also studied the Raman shift of *c*-BN at pressure up to 21 GPa and temperatures up to 700 K, however, studies of the Raman shift of *c*-BN at simultaneous high-P and high-T conditions are still rare, giving rise to larger deviation in the existing *c*-BN P-T sensor, especially at high-temperature conditions (> 700 K). The lack of reliable calibration could lead to either an underestimation or overestimation of pressure from *c*-BN Raman shift P-T sensor.

Here, we systematically studied in-situ Raman shift of *c*-BN (TO mode) at room-pressure and high-temperature (1 bar, 293 - 1300 K), room-temperature and high-pressure (293 K, 1 bar - 46 GPa), and high-temperature and high-pressure (293 - 1100 K, 1 bar - 15 GPa), respectively. We established a *c*-BN Raman shift P-T sensor, which can be used to accurately determine the pressure and/or temperature in the DAC at least up to 15 GPa and 1300 K. Furthermore, we conducted three sets of high P-T experiments to test the practicability of *c*-BN sensor in the water-rock interaction experiments up to 5 GPa and 1023 K.

2. EXPERIMENTAL METHODS

The pure synthetic *c*-BN powders were ordered from Zhengzhou Zhongnan JETE Superrabrasives Co., LTD, Henan, China, whose shock compression behavior has been studied by Hu et al. (2018). Both the ruby sphere (BETSA company, France) and Sm^{2+}:SrB_4O_7 powders (synthesized by Zhao et al. 2016) were used as internal standards to calibrate the Raman shift P-T sensor of *c*-BN.

2.1 In-situ Raman measurements

In-situ Raman spectra were collected from a diamond window of the DAC or a sapphire window of the heating stage under the Renishaw Raman system (RM1000) at HPSTAR. The 532 nm line of Nd:YAG laser was used as the excitation source. The Raman signal of the Si metal line at 520 cm^{-1} was used to calibrate the Raman system

before and after each measurement. By comparing the Raman shift on the same *c*-BN grain under different laser power, we found that *c*-BN grains could be heated due to the absorption of laser light, which may result in a significant Raman shift. The Raman shift was systematically analyzed for *c*-BN grains with different sizes (8 - 90 μm) using different laser power (4 - 20 mW). Finally, the laser power of the Raman system below 5 mW on *c*-BN grains was used for this calibration and later water-rock interaction experiments. The measurements at each P-T condition were performed after equilibrating the system for 5-10 minutes to obtain a steady-state Raman frequency.

2.2 Room-P and high-T experiments

A heating stage (HRTS1000; Shanghai Photographic Instrument Co., Ltd) with a sapphire window was used to heat samples at ambient pressure. The thermocouple is buried under the center of the reaction chamber of the heating stage. To obtain an accurate experimental temperature, we used several metals (e.g., 63A solder, tin, zinc, and silver) with well-known melting points (183 °C, 232 °C, 420 °C, and 961 °C) to calibrate the real temperature of the heating stage (Fig. S2a) before calibration experiments (Yang et al. 1993). The temperature of the heating stage (actual temperature) on the sample position in the reaction chamber was calibrated from room T to 1000 ℃. Particles of 0.2 - 0.5 mm^2 of each metal material were pre-indented into thin foils with a diameter of 0.5 mm to 1 mm (Fig. S2b), and then loaded into the center of the heating

192 stage reaction chamber. External cooling water at 20 °C was used to protect the whole
193 heating state body from high temperature. A protective hydrogen-argon mixture gas (98 %
194 Ar + 2 % H_2) was slowly blown into the reaction chamber to avoid any oxidation of the
195 metal samples by air. The heating rate was set to be 5 °C / min during the heating process.
196 When the instantaneous shrinkage of a metal foil was observed under the microscope, a
197 real temperature was recorded. In most cases, the shrinkage time of the metal foils was
198 less than 2 s and the temperature interval was less than 0.1 °C (Fig. S2b). The calibration
199 processes were repeated several times to ensure that the calibration deviation was less
200 than 1 °C. Based on the temperature difference between the controller of the heating stage
201 and the real temperature (i.e., the known meting temperature of the given metal), we
202 corrected the controller temperature by linear fitting (Fig. S2c).
203

204 **2.3 Room-T and high-P & high-T and high-P experiments**

205 Both room-T and high-P experiments & high-P and high-T experiments were carried
206 out in a high-temperature BX-90 DAC equipped with two IIa diamond anvils. The culet
207 diameter of diamond anvils was 500 μm or 250 μm, depending on the target pressure (i.e.,
208 500 μm for experimental pressure below 16 GPa, 250 μm for the experimental pressure
209 from 16 GPa to 46 GPa). For the room-T and high-P experiment, high-pressure (0.16 GPa)
210 pure helium gas was filled into the reaction chamber as pressure media using a high-

211 pressure gas loader at HPSTAR. Several *c*-BN crystals, ruby spheres, and Sm^{2+}:SrB_4O_7
212 powders were loaded together into a 100 μm hole in the rhenium gasket (Fig. S3). For
213 high-T and high-P experiments, the same pressure transmitting medium as room-T and
214 high-P experiment has been used, an external resistance heater of Ni-Cr wire was placed
215 around diamond anvils for heating samples (Figs. S3a, S3b), and the temperature was
216 measured with a K-type thermal couple mounted to one of the diamond anvils by high-
217 temperature cement (Fig. S3c). The temperature deviation in the DAC reaction chamber
218 was checked by the melting points of tin (232 °C) within 2 °C. The experimental pressure
219 was calculated by fluorescence shift of the ruby sphere (Mao et al. 1986) and/or the
220 Sm^{2+}:SrB_4O_7 powders (Datchi et al. 2007) as below:

221 $$P_{R1} = 248.4[\left(\frac{\Delta\lambda}{\lambda_0}\right)^{7.665} - 1]$$ (Mao et al. 1986) (1)

222 $$P_{0-0} = 3.9096\Delta\lambda\frac{1+0.03378\Delta\lambda}{1+0.0105\Delta\lambda}$$ (Datchi et al. 2007) (2)

223 Where P is in GPa and λ is in nm. λ is the fluorescence shift of the ruby (R1) or
224 Sm^{2+}:SrB_4O_7 (0–0) Lines, and λ_0 is the initial wavelength at ambient conditions (293 K, 1
225 atm). Here, λ_0 = 693.973 (13) nm for ruby, $\lambda_{0\text{-}0}$ = 685.125 (9) nm for Sm^{2+}:SrB_4O_7, and
226 $\Delta\lambda = \lambda\ (P, T) - \lambda_0$. Previous studies usually ignored the temperature effect for the
227 Sm^{2+}:SrB_4O_7 P-T sensor because of its minimal effect on the 0–0 line shift (Lacam and
228 Chateat 1989; Leger et al. 1990; Raju et al. 2011; Fig. S4a and S4b). Here, we re-fitted
229 the temperature dependence of fluorescence shift of the Sm^{2+}:SrB_4O_7 at high

temperatures (Fig. S5). In order to obtain a more accurate pressure value than before, we also deducted the fluorescence shift caused by temperature when calculating the pressure by the Sm^{2+}:SrB_4O_7 sensor. In Fig. S5, we compared the results with linear fitting from Lacam et al. (1989), Raju et al. (2011), and Jing et al. (2013) where they give a slope of -1×10^{-4} , 2×10^{-5} and -2×10^{-4} nm / K respectively. Datchi et al. (2007) used a nonlinear equation of $\Delta\lambda_{0\text{-}0} = 8.7\ (12) \times 10^{-5}\ \Delta T + 4.62(60) \times 10^{-6}\Delta T^2 - 2.38(70)\times 10^{-9}\Delta T^3$. Our experimental result is more consistent with that from Datchi et al. (2007). Therefore, we used the Sm^{2+}:SrB_4O_7 pressure scale formula reported by Datchi et al. (2007) to improve the pressure calibration of the TO mode of *c*-BN in this study. The big difference between our study and other studies (Lacam et al. 1989; Raju et al. 2011; Jing et al. (2013) may result from different laser power used for the Raman system (see below for more detailed discussions). In this study, the pressure deviations given by two independent standards (ruby and Sm^{2+}:SrB_4O_7) are consistently kept within ± 5%, indicating that the calibrated *c*-BN P-T sensor in this study is internally consistent with ruby and Sm^{2+}:SrB_4O_7 in our experimental P-T ranges.

In total, 108 measurements at 54 P-T conditions were collected from ambient conditions to high-T and high-P conditions up to 1300 K and 46 GPa for *c*-BN P-T sensor calibration in this study (Table S1). To test the practicability of *c*-BN in the water-rock interaction experiment, we carried out three sets of DAC experiments to characterize the

changes of different pressure sensors (e.g., *c*-BN, Sm^{2+}:SrB_4O_7, and ruby) in the water-quartz system at high-P and high-T conditions up to 5 GPa and 1023 K. The Raman peaks of *c*-BN at different P-T conditions were fitted with the symmetric Gauss + Lorentz function after subtracting a linear baseline. All fitting parameters (e.g., peak positions) are summarized in Table S1.

3. RESULTS AND DISCUSSION

3.1 Temperature-dependent Raman shift of *c*-BN

We measured *c*-BN Raman spectra from room T to 1223 K with 50 K intervals at room pressure (Fig. 1a) and obtained a relationship between the Raman shift and temperature (Fig. 1b). The *c*-BN LO mode gradually weakens and disappears with an increase of temperature to ~ 1100 K. However, the TO mode peak of *c*-BN remains in good shape in all high-temperature experiments (Fig. 1a), and is used to fit the correlation between the Raman shift and temperature by the polynomial equation as below:

$$\nu_{TO}(P = 0, T) = 1054.58(16) - 0.02206(71)\,T - 1.1000(70) \times 10^{-5}\,T^2 \quad (R^2=0.999) \quad (3)$$

As shown in Fig. 1b, our fitted curve is well included in the previous study and R^2 is 0.999. The temperature dependences of Raman shift of *c*-BN at ambient pressure have been investigated in previous studies (Alvarenga et al., 1992; Herchen and Capelli, 1993; Datchi and Canny, 2004). A comparison for the temperature-induced Raman shift of *c*-

268 BN is shown in Table 1. In comparison with previous studies, our results are in good
269 agreement with Datchi and Canny (2004) in the low-temperature range (< 600 K) (Fig.
270 1b), however, there is a slight deviation above 600 K due to limited data (less than 723 K)
271 from Datchi and Canny (2004). The *c*-BN Raman shift from earlier works (e.g.,
272 Alvarenga et al. 1992 and Herchen and Cappelli 1993) are systematically deviating from
273 our data at the same temperature conditions, which may be due to an overall shift of the
274 early Raman spectrometer or different laser power used for a different measurement. The
275 heating equipment used by Alvarenga et al. (1992) and Herchen and Capelli (1993) were
276 not systematically calibrated before use at high temperature (see calibration in section
277 2.2), which may also result in significant uncertainty in the experimental temperature.
278 Alvarenga et al. (1992) obtained a linear Raman shift of *c*-BN with temperature with a
279 slope at -0.038(2) cm^{-1}/K from 300 to 1600 K, whereas Herchen and Capelli (1993) found
280 a nonlinear behavior from 300 to 1840 K. However, we re-fitted the data of Alvarenga et
281 al. (1993) and found that the TO frequency and temperature can be better expressed as a
282 non-linear relationship in Fig. 1b. The goodness of fit (R^2) is 0.951 for the linear
283 expression and 0.969 for the polynomial expression indicating that Alvarenga et al. (1993)
284 may have used the improper function to fit the relationship between the TO frequency
285 and temperature. On the other hand, the different initial Raman shift value and irregular
286 evolution of *c*-BN Raman shift with temperature in early works (e.g., Alvarenga et al.

1992; Herchen et al. 1993) may result from excessive laser heating (see discussion in section 3.4).

3.2 Pressure-dependent Raman shift of *c*-BN

The systematical Raman shift of *c*-BN with increasing pressure at room temperature is shown in Fig. 2a. The correlation between the Raman shift and pressure from 1 bar to ~ 46 GPa are fitted as a polynomial in Fig. 2b in comparison with that from previous studies (Sanjurjo et al., 1983; Datchi and Canny; 2004; Ono et al., 2015). Sanjurjo et al. (1983) studied the pressure dependence of *c*-BN Raman shift at room temperature up to 8.2 GPa using a 4:1 methanol-ethanol mixture as a pressure medium in a DAC, and a linear function with a slope at 3.39 (8) cm^{-1}/GPa was chosen to fit experimental data. Datchi and Canny (2004) studied the pressure-dependent Raman shift of *c*-BN up to 21 GPa in a helium gas pressure medium in a DAC and found a linear migration rate of 3.27(2) cm^{-1}/GPa below 10 GPa, but a nonlinear relationship at higher pressure. In addition, Ono et al. (2015) extended experimental pressure up to 90 GPa using NaCl as a pressure medium, with a dν/dP slope at 3.41(7) and 2.04(7) cm^{-1}/GPa at 1 bar and 90 GPa, respectively.

In this study, *c*-BN Raman shift can be well linearly fitted with a variation of 3.35 (3) cm^{-1}/GPa below 10 GPa, which is pretty consistent with that from previous studies (Sanjurjo et al. 1983; Datchi and Canny 2004; Ono et al. 2015). When the pressure is below 25 GPa, the difference in pressure between linear and polynomial functions is relatively small. However, if the linear fitting of Sanjurjo et al. (1983) is extrapolated to high pressure (> 25 GPa), the difference between Sanjurjo et al. (1983) and our study increases rapidly as the pressure increases. This is the fatal uncertainty of pressure calibration. Our experimental results are consistent with Ono et al. (2015) as well, the slight difference above 25 GPa may attribute to non-hydrostatic NaCl pressure media used by Ono et al. (2015), which may undergo a phase transformation from B1- to B2-type at 25 GPa. The correlation between the Raman shift and pressure is clearly non-linear, which can be well reproduced as below (Fig. 2b):

$$\nu_{TO}(P, T = 293K) = 1055.37(18) + 3.35(2)P - 0.011(1)P^2 \quad (R^2=0.999) \quad (4)$$

3.3 Coupled effect of P-T on *c*-BN Raman shift

To test the coupled effect of pressure and temperature on the Raman shift of *c*-BN in this study, we carried out seven sets of high-temperature and high-pressure experiments in the DAC (Fig. S6). During the heating process, both the volume expansion of the reaction chamber in the DAC and hole deformation in the Re gasket affected the pressure changes on the samples at high-temperature and high-pressure conditions.

This is the peer-reviewed, final accepted version for American Mineralogist, published by the Mineralogical Society of America.
The published version is subject to change. Cite as Authors (Year) Title. American Mineralogist, in press.
DOI: https://doi.org/10.2138/am-2022-8372. http://www.minsocam.org/

Combining all the data we obtained from room pressure and high temperature, room temperature and high pressure (here pressure less than 15 GPa was selected), and high temperature and pressure experiments, we fitted the curved surface of Raman shift (ν_{TO}) using a best polynomial expression (Fig. 3) as the following equation:

$$\Delta\nu_{TO}(P,T) = 2.81(51) - 0.0053(16)T - 1.78\times10^{-5}(11)T^2 + 3.47(6)P - 0.055(6)P^2 + 0.00105(7)P\cdot T \quad (R^2=0.998) \qquad (5)$$

$\Delta\nu_{TO(P,T)}$ is the difference of Raman shift between high-P and/or high-T conditions of interest [$\nu_{TO}(P, T)$] and the reference at ambient conditions [$\nu_0(P_0, T_0]$. Eq. 5 shows that the Raman shift of *c*-BN is a coupled function of pressure and temperature, rather than a simple linear superposition of pressure and temperature, indicating a significant P-T cross derivative term on *c*-BN sensor.

The fitting surface can be used to determine the pressure from the Raman shift of *c*-BN at a given temperature if Eq. 5 is converted to Eq. 6 as below:

$$P = \frac{A(T)-\sqrt{A(T)^2+0.2194B(T,\Delta\nu)}}{0.1097} \qquad (6)$$

$$A(T) = 3.47\,(6) + 0.00105\,(7)T, B(T,\Delta\nu) = 2.81\,(51) - 0.0053\,(16)\,T - 1.78\,(11)\times10^{-5}\,T^2 - \Delta\nu_{TO}.$$

We compared pressure determined from the Sm^{2+}:SrB_4O_7 by Eq. 2 and from *c*-BN by Eq. 6 at high temperature in Table S1. It shows that almost all deviations between pressure determined from the Sm^{2+}:SrB_4O_7 by Eq. 2 and *c*-BN by Eq. 7 are within 3%.

Only several points at low pressure are above 10% because of the relatively small denominator (the pressure determined from the Sm^{2+}:SrB_4O_7 by Eq. 2), indicating that an accurate pressure at high-temperature can be determined by using Raman shift P-T sensor of *c*-BN in this study. Datchi and Canny (2004) also calibrated the temperature- and pressure-dependent Raman shift of *c*-BN up to 700 K and 21 GPa. They fitted all experimental data over the whole P-T range as:

$$P = -43.4783\{\mathrm{A(T)} + \sqrt{\mathrm{A(T)} - 0.046[\nu_{\mathrm{TO}}(\mathrm{P,T}) - \mathrm{B(T)}}\} \quad (7)$$

$$\mathrm{A(T)} = 3.325\ (11) - 0.00022\ \mathrm{T}, \mathrm{B(T,\Delta\nu)} = 1058.4\ (2) - 9.6\ (7)\ \times\ 10^{-3}\ \mathrm{T} - 1.54\ (7)\ \times\ 10^{-5}\ \mathrm{T}^2.$$

We compared the pressure derivation ΔP(%) = (P1-P2)/P1*100% between Eq. 6 from this study and Eq. 7 from Datchi and Canny (2004) at different experimental temperatures and pressure (Fig. 4). As Fig. 4a showed, the pressure derivation between Eq. 6 in this study and Eq. 7 is less than 15% in our experimental pressure range. However, Fig. 4b showed that with an increase of experimental temperature, the pressure given by Eq. 7 from Datchi and Canny (2004) seems to overestimate pressure because the cross-derivative term of both the pressure and temperature is underestimated in their study. The coupling effect coefficient ($\frac{\partial^2 \nu_{\mathrm{TO}}}{\partial \mathrm{P}\,\partial \mathrm{T}} = 0.000222$) from Eq. 7 (Datchi and Canny 2004) is smaller than Eq. 6 ($\frac{\partial^2 \nu_{\mathrm{TO}}}{\partial \mathrm{P}\,\partial \mathrm{T}} = 0.00105(7)$) in this study. Therefore, pressure deviation cannot be ignored for the Raman shift P-T sensor of *c*-BN, especially at high-

362 temperature conditions. Further, we also extended the Raman shift of *c*-BN in a higher
363 temperature range from 700 K in Datchi and Canny (2004) to 1300 K in this study. The
364 Raman shift P-T sensor of *c*-BN in this study could fill the gap of P-T sensors ranging
365 from externally resistance-heated to laser-heated DAC experiments.
366
367
368 **3.4 Effect of laser power and grain size on Raman shift of *c*-BN**
369 During calibration experiments, we found that *c*-BN grains can be heated due to the
370 absorption of laser light of the Raman system, which may result in a significant Raman
371 shift of *c*-BN. The Raman shift of the TO mode for *c*-BN may change from 1054 cm^{-1} to
372 1045 cm^{-1} with laser power increasing from 1 to 20 mw at room pressure (Fig. 5).
373 Therefore, it is necessary to control the Raman shift caused by laser heating. Thus, we
374 recommend using laser power as low as possible to avoid deviations caused by heat
375 absorption when using *c*-BN to be a P-T sensor. On the other hand, Werninghaus et al.
376 (1997) also reported that grain size effects, such as the presence of nanocrystalline *c*-BN
377 or amorphous BN, will cause a significant Raman shift. In order to explore the influence
378 of grain size on *c*-BN Raman shift, we also compared Raman shift of *c*-BN with grain
379 sizes of 8 - 12 μm, 38 - 45 μm, 53 - 63 μm, and 75 - 90 μm using different laser power,
380 respectively (Fig. 5). We linearly fitted the correlation between the Raman shift of *c*-BN

and the laser power for different grain sizes (Fig. 5). In summary, we found that there is a systematical non-negligible Raman shift of *c*-BN with different sizes under the same laser power (Fig. 5). The larger the grain size of *c*-BN is, the less thermal effect was observed. Frurthermore, the effect of laser power on the Raman shift of *c*-BN can be linearly fitted with a negative slope, which is the same as the temperature effect we discussed before (section 3.1).

In summary, the grain size of *c*-BN should be as large as possible for better heat dissipation, while the laser power should be as small as possible (< 5 mW) to avoid heating of *c*-BN grains, if we choose *c*-BN as the P-T sensor for DAC experiments.

4. Application of *c*-BN P-T sensor to water-rock interaction experiments

In the first testing experiment, two *c*-BN crystals and a piece of quartz crystal were loaded in the sample chamber with water as the pressure medium (Fig. 6). Experimental pressure is determined by the Raman shift of *c*-BN using Eq. 6. We also calculate the pressure in the sample chamber by using Raman shift P-T sensor of quartz from Schmidt et al. (2000) at the low-pressure range (< 2 GPa). The pressure calculated from *c*-BN (1.83 GPa) is in good agreement with that from the quartz P-T sensor (1.68 GPa), which further indicates the reliability of *c*-BN Raman shift P-T sensor in this study. During heating, we observed the quartz crystal become smaller and the Raman intensity of the

400 quartz gradually weakened until completely disappeared at the temperature of 1023 K,
401 indicating quartz dissolves in water with the increase of temperature. However, the
402 Raman intensity of *c*-BN did not get weak with an increase of temperature or pressure in
403 our experimental temperature and pressure range. The *c*-BN crystals maintain a good
404 crystal form before and after high-temperature and high-pressure experiments, indicating
405 that no dissolution of *c*-BN in water occurs at high P-T conditions. Therefore, we have
406 reason to believe that *c*-BN has very stable properties in water and can accurately
407 determine the pressure in DAC at high-temperature and high-pressure conditions up to
408 1023 K and 5.00 GPa or higher.

409 In the second testing experiment, a piece of quartz crystal and some Sm^{2+}:SrB_4O_7
410 powders were placed in the sample chamber with water (Fig. 7). The pressure is
411 determined by the fluorescence shift of Sm^{2+}:SrB_4O_7 using Eq. 2. The pressure calculated
412 from Sm^{2+}:SrB_4O_7 (1.32 GPa) is also in good agreement with that from quartz (1.41 GPa)
413 by Schmidt et al. 2000. With the increase of temperature, both Sm^{2+}:SrB_4O_7 and quartz
414 showed an obvious dissolution phenomenon, and Raman intensities of quartz and
415 Sm^{2+}:SrB_4O_7 gradually weakened. The temperature for the complete dissolution of quartz
416 is between 873 K and 1023 K, and the temperature when Sm^{2+}:SrB_4O_7 is completely
417 dissolved is between 673 K and 1023 K. The reaction or dissolution of quartz or

418 Sm^{2+}:SrB_4O_7 in water at high temperatures makes it hard to obtain a Raman signal, thus
419 cannot be used as pressure sensors at these P-T conditions.

420 In the third testing experiment, a piece of quartz crystal and a ruby sphere were
421 loaded in the sample chamber with water (Fig. 8). The pressure calculated from ruby
422 using Eq. 1 (1.44 GPa) is also in good agreement with that from the quartz P-T sensor
423 (1.41 GPa) by Schmidt et al. (2000). With the increase of temperature, the quartz
424 completely dissolved in water at 673 K. The linewidth of the fluorescence lines of ruby
425 rapidly increases with temperature, and the doublet R1–R2 becomes a broad, unresolved
426 band above~573 K (Fig.S1, Fig. 8), which makes it impossible to obtain the real pressure.
427 Further, the stronger fluorescence of ruby at high temperature could cover the Raman
428 signal of the fluid in the sample chamber of DACs as well. Therefore, ruby is also not a
429 suitable pressure sensor for most of the water-rock interaction experiments in DAC at
430 high temperatures.

431 In summary, we found that *c*-BN Raman shift P-T sensor has a big advantage in the
432 determination of pressure for water-rock interaction experiments in DAC. Raman shift of
433 *c*-BN is an ideal P-T sensor for water-rock reaction experiments at high-temperature and
434 high-pressure conditions relevant to subduction zones.

435 **5. CONCLUSION AND IMPLICATION**

436 We have systematically studied the Raman shift of *c*-BN up to 46 GPa and 1300 K.
437 To our knowledge, this is the first report of Raman shift of *c*-BN at simultaneous high-
438 pressure and high-temperature (>700 K) conditions. Our experimental results showed that
439 Raman shift of *c*-BN is a coupled function of pressure and temperature (i.e., $\frac{\partial^2 \nu_{TO}}{\partial P\, \partial T} =$
440 0.00105(7)), which is ignored in previous studies. Further, we tested and discussed the
441 influence of grain size and laser power on Raman peak shift of *c*-BN and found that the
442 grain size should be as large as possible and the laser power should be as small as
443 possible when using *c*-BN as a P-T sensor in DAC. The testing experiments of water-rock
444 reaction in this study showed *c*-BN P-T sensor can successfully determine the accurate
445 pressure in water-rock reaction experiments in DAC at high temperature and high
446 pressure up to 1023 K and 5.00 GPa or higher. Finally, combining the inert chemical
447 activity of *c*-BN and its distinguishable Raman signal from the diamond anvil at high-P
448 and high-T conditions, we propose that *c*-BN will be an ideal P-T sensor for studying
449 water-rock interactions in a DAC at high-pressure and high-temperature conditions
450 relevant to subduction zones. The *c*-BN P-T sensor will be very useful for experimenters
451 who want to investigate fluid properties in high-pressure metamorphic rocks (e.g.,
452 eclogite or granulite) in subduction zones.
453

454 **ACKNOWLEDGMENTS**

455 This study was supported by the National Key Research and Development Program
456 of China (2019YFA0708501) and the NSFC Major Research Plan on West-Pacific Earth
457 System Multispheric Interactions (project number: 92158206). We thank Xiaojun Hu
458 from the Wuhan University of Technology for kindly providing the synthetic *c*-BN
459 powders and Dr. Chaoshuai Zhao and Prof. Heping Li for providing the synthetic
460 Sm^{2+}:SrB_4O_7 powders for the calibration work in this study. We also thank two
461 anonymous reviewers for their constructive comments and Dr. Antonio dos Santos
462 (Associate Editor) for his careful editorial handling and helpful suggestions.

463

464

465 **REFERENCES CITED**

466 Albe, K. (1997) Theoretical study of boron nitride modifications at hydrostatic pressures.
467 Physical Review B, 55(10), 6203.

468 Andreani, M., Daniel, I., and Pollet-Villard, M. (2013) Aluminum speeds up the
469 hydrothermal alternation of olivine. American Mineralogist, 98, 1738–1744.

470 Alvarenga, A., Grimsditch, M., and Polian, A. (1992) Raman scattering from cubic boron
471 nitride up to 1600 K. Journal of Applied Physics, 72, 1955-1956.

Aleksandrov, I.V., Goncharov, A.F., Stishov, S.M., and Iakovenko, E.V. (1989) Equation of state and Raman scattering of light in cubic BN and SiC at high pressures. Pisma v Zhurnal Eksperimentalnoi i Teoreticheskoi Fiziki, 50, 116-120.

Barnett, J.D., Block, S., and Piermarini, G.J. (1973) An optical fluorescence system for quantitative pressure measurement in the diamond-anvil cell. Review of Scientific Instruments, 44, 1–9.

Cui, H., Zhong, R., Wang, X., Li, Z., and Chen, H. (2020) Reassessment of the zircon Raman spectroscopic pressure sensor and application to pressure determination of fused silica capillary capsule. Ore Geology Reviews, 122.

Datchi, F., Loubeyre, P ., and LeToullec, R. (2000) Extended and accurate determination of the melting curves of argon, helium, ice (H_2O), and hydrogen (H_2). Physical Review B, 61, 6535–6546.

Datchi, F., Letoullec, R., and Loubeyre, P. (1997) Improved calibration of the $Srb_4O_7:Sm^{2+}$ optical pressure gauge: advantages at very high pressures and high temperatures. Journal of Applied Physics, 81(8), 3333-3339.

Datchi, F. and Canny, B. (2004) Raman spectrum of cubic boron nitride at high pressure and temperature. Physical Review B, 69, 144106.

489 Datchi, F., Dewaele, A., Loubeyre, P., LeToullec, R., Le Godec, Y., and Canny, B. (2007)
490 Optical pressure sensors for high-pressure–high-temperature studies in a diamond
491 anvil cell. High Pressure Research, 27, 447–463.
492 Dobrzhinetskaya, L., Wirth, R., Yang, J., Hutcheon, I., Weber, P., and Green, H. (2009)
493 High-pressure highly reduced nitrides and oxides from chromitite of a Tibetan
494 ophiolite. Proceedings of the National Academy of Sciences, 106, 19233 - 19238.
495 Dorogokupets, P.I., and Oganov, A.R. (2007) Ruby, metals, and MgO as alternative
496 pressure scales: a semiempirical description of shock-wave, ultrasonic, x-ray, and
497 thermochemical data at high temperatures and pressures. Physical Review B, 75,
498 024115.
499 Facq, S., Daniel, I., Montagnac, G., Cardon, H., and Sverjensky, D.A. (2014) In situ
500 Raman study and thermodynamic model of aqueous carbonate speciation in
501 equilibrium with aragonite under subduction zone conditions. Geochimica Et
502 Cosmochimica Acta, 132, 375-390.
503 Facq, S., Daniel, I., Montagnac, G., Cardon, H., and Sverjensky, D.A. (2016) Carbon
504 speciation in saline solutions in equilibrium with aragonite at high pressure.
505 Chemical Geology, 431, 44-53.

506 Farsang, S., Facq, S., and Redfern, S. (2018) Raman modes of carbonate minerals as
507 pressure and temperature gauges up to 6 GPa and 500 °C. American Mineralogist,
508 103, 1988 - 1998.
509 Farsang, S., Widmer, R.N., and Redfern, S. (2021) High-pressure and high-temperature
510 vibrational properties and anharmonicity of carbonate minerals up to 6 GPa and
511 500 °C by Raman spectroscopy. American Mineralogist, 106(4), 581-598.
512 Fei, Y., Ricolleau, A., Frank, M., Mibe, K., Shen, G., and Prakapenka, V. (2007) Toward
513 an internally consistent pressure scale. Proceedings of the National Academy of
514 Sciences of the United States of America, 104(22), 9182-9186.
515 Goncharov, A.F., Zaug, J.M., Crowhurst, J.C., and Gregoryanz, E. (2005) Optical
516 calibration of pressure sensors for high pressures and temperatures. Journal of
517 Applied Physics, 97.
518 Goncharov, A. F., Sinogeikin, S., Crowhurst, J. C., Ahart, M., Lakshtanov, D.,
519 Prakapenka, V., and Fei, Y. (2007). Cubic boron nitride as a primary calibrant for a
520 high temperature pressure scale. High Pressure Research, 27(4), 409-417.
521 Herchen, and Cappelli (1993) Temperature dependence of the cubic boron nitride Raman
522 lines. Physical review. B, Condensed matter, 47 21, 14193-14199.

523 Hu, X., Yang, G., Zhao, B., Li, P., Yang, J., Leng, C., Liu, H., Huang, H., Fe ,Y .(2018)
524 Shock compression behavior of a mixture of cubic and hexagonal boron nitride.
525 Journal of Applied Physics, 123(17), 175903.
526 Hess, N.J. and Schiferl, D. (1990) Pressure and temperature dependence of laser-induced
527 fluorescence of Sm:YAG to 100 kbar and 700°C and an empirical model. Journal of
528 Applied Physics, 68(5), 1953-1960.
529 Jing, Q., Wu, Q., Liu, Y., Zhang, Y., Liu, S., Liu, L., Xu, J., and Bi, Y. (2013) Effect of
530 pressure and temperature on the wavelength shift of the fluorescence line of
531 $SrB_4O_7:Sm^{2+}$ scale. High Pressure Research, 33, 725 - 733.
532 Kantor, I., Prakapenka, V., Kantor, A., Dera, P., Kurnosov, A., Sinogeikin, S., and
533 Dubrovinsky, L. (2012) BX90: A new diamond anvil cell design for X-ray
534 diffraction and optical measurements. Review of Scientific Instruments, 83(12),
535 125102.
536 Lv, Meizhe., Bin., Cai., Lichao., Guo., and Xiaofei. (2018) Auger electron spectroscopy
537 analysis for growth interface of cubic boron nitride single crystals synthesized under
538 high pressure and high temperature. Applied Surface Science: A Journal Devoted to
539 the Properties of Interfaces in Relation to the Synthesis and Behaviour of Materials,
540 439(May 1), 780-783.

Lacam, A., and Chateau, C. (1989) High-pressure measurements at moderate temperatures in a diamond anvil cell with a new optical sensor: $SrB_4O_7:Sm^{2+}$. Journal of Applied Physics, 66, 366-372.

Leger, J., Chateau, C., and Lacam, A. (1990) $SrB_4O_7:Sm^{2+}$ pressure optical sensor: investigations in the megabar range. Journal of Applied Physics, 68, 2351-2354.

Mao, H.K., Bell, P.M., Shaner, J.W., and Steinberg, D.J. (1978) Specific volume measurements of Cu, Mo, Pd, and Ag and calibration of the ruby R1 fluorescence pressure gauge from 0.06 to 1 mbar. Journal of Applied Physics, 49(6), 3276-3283.

Mao, H.K., Xu, J., and Bell, P.M. (1986) Calibration of the ruby pressure gauge to 800 kbar under quasi-hydrostatic conditions. Journal of Geophysical Research, 91, 4673–4676.

Manning, C.E. (1994) The solubility of quartz in H_2O in the lower crust and upper mantle. Geochimica et Cosmochimica Acta, 58, 4831–4839.

Ono, S., Mibe, K., and Ohishi, Y. (2014) Raman spectra of culet face of diamond anvils and application as optical pressure sensor to high temperatures. Journal of Applied Physics, 116(5), 2340.

Ono, S., Mibe, K., Hirao, N., and Ohishi, Y. (2015) In situ Raman spectroscopy of cubic boron nitride to 90 Gpa and 800 K. Journal of Physics & Chemistry of Solids, 76, 120-124.

560 Piermarini, G.J., Block, S., Barnett, J.D., and Forman, R.A. (1975) Calibration of the
561 pressure dependence of the R1 ruby fluorescence line to 195 kbar. Journal of
562 Applied Physics, 46(6), 2774-2780.
563 Ragan, D.D., Gustavsen, R., and Schiferl, D. (1992) Calibration of the ruby R1 and R2
564 fluorescence shifts as a function of temperature from 0 to 600 K. Journal of Applied
565 Physics, 72, 5539–5544.
566 Raju, S.V., Zaug, J. M., Chen, B., Yan, J., Knight, J. W., and Jeanloz, R. (2011)
567 Determination of the variation of the fluorescence line positions of ruby, strontium
568 tetraborate, alexandrite, and samarium-doped yttrium aluminum garnet with pressure
569 and temperature. Journal of Applied Physics, 110(2), 6744.
570 Rashchenko, S.V., Kurnosov, A., Dubrovinsky, L., and Litasov, K. D. (2015) Revised
571 calibration of the Sm^{2+}:SrB_4O_7 pressure sensor using the Sm-doped yttrium-
572 aluminum garnet primary pressure scale. Journal of Applied Physics, 117(14),
573 145902.
574 Schmidt, C., and Ziemann, M. A. (2000) In-situ Raman spectroscopy of quartz: A
575 pressure sensor for hydrothermal diamond-anvil cell experiments at elevated
576 temperatures. American Mineralogist, 85(11-12), 1725-1734.

577 Schmidt, C., Steele-MacInnis, M., Watenphul, A., and Wilke, M. (2013) Calibration of
578 zircon as a Raman spectroscopic pressure sensor to high temperatures and
579 application to water-silicate melt systems. American Mineralogist, 98, 643 - 650.
580 Shen, Y.R., Gregorian, T., and Holzapfel, W.B. (1991) Progress in pressure
581 measurements with luminescence sensors. High Pressure Research, 7(1-6), 73-75.
582 Sanjurjo, J.A., López-Cruz, E., Vogl, P., and Cardona, M. (1983) Dependence on volume
583 of the phonon frequencies and the IR effective charges of several III-V
584 semiconductors. Physical Review B, 28(8), 4579.
585 Tardieu, A., F Cansell, and Petitet, J.P. (1990) Pressure and temperature dependence of
586 the first-order Raman mode of diamond. Journal of Applied Physics, 68(7), 3243-
587 3245.
588 Tropper, P., and Manning, C.E. (2007) The solubility of corundum in H_2O at high
589 pressure and temperature and its implications for Al mobility in the deep crust and
590 upper mantle. Chemical Geology, 240, 54–60.
591 Trots, D.M., Kurnosov, A., Ballaran, T.B., Tkachev, S., Zhuravlev, K., Prakapenka, V.,
592 and Frost, D.J. (2013) The Sm: YAG primary fluorescence pressure scale. Journal of
593 Geophysical Research: Solid Earth, 118(11), 5805-5813.
594 Wentorf, R.H. (1957) Cubic form of boron nitride. Journal of Chemical Physics, 26(4),
595 956-956.

596 Watenphul, A., and Schmidt, C. (2012) Calibration of berlinite ($AlPO_4$) as Raman
597 spectroscopic pressure sensor for diamond-anvil cell experiments at elevated
598 temperatures. Journal of Raman Spectroscopy, 43, 564–570.
599 Werninghaus, T., Hahn, J., F Richter, and Zahn, D. (1997) Raman spectroscopy
600 investigation of size effects in cubic boron nitride. Applied Physics Letters, 70(8),
601 958-960.
602 Yang, Y., Zhang, K., Cui, X. (1993) Relation between the Heat of Fusion and the Melting
603 Point of Metal. Journal of Inner Mongolia University of Technology (Natural
604 Science), 02.
605 Zhang, W. J., and Matsumoto, S. (2001) Investigations of crystallinity and residual stress
606 of cubic boron nitride films by Raman spectroscopy. Physical Review B, 63(7), 247-
607 250.
608 Zhao, C., Li, H., Wang, Y., Jiang, J., and He, Y. (2017) $SrB_4O_7:Sm^{2+}$: an optical sensor
609 reflecting non-hydrostatic pressure at high-temperature and/or high pressure in a
610 diamond anvil cell. High Pressure Research, 37, 18–27.
611 Zhao, Y., Barvosa-Carter, W., Theiss, S.D., Mitha, S., Aziz, M. J., and Schiferl, D. (1998)
612 Pressure measurement at high temperature using ten Sm:YAG fluorescence peaks.
613 Journal of Applied Physics, 84(8), 4049-4059.
614

615

616

617

618 **FIGURES CAPTIONS**

619 **Figure 1:** (a) Evolution of the TO and LO Raman mode of *c*-BN with changing
620 temperatures at room pressure. (b) Raman shifts of the TO mode of *c*-BN as a function of
621 temperature at room pressure in this study in comparison with that from previous studies
622 (Datchi and Canny (2004); Alvarenga et al. (1992); Herchen and Capelli (1993)). The red
623 dotted line, blue dotted line and black dotted line are the data fitting results of this study,
624 Datchi and Canny (2004) and Herchen and Capelli (1993), respectively. The green
625 straight line and the green dotted dashed line are linear fitting and polynomial fitting of
626 the results of Alvarenga et al. 1992, respectively. Error bars are smaller than symbols.

627 **Figure 2:** (a) Evolution of the TO mode Raman spectra of *c*-BN at different pressures at
628 room temperature. (b) Raman shifts of the TO mode of *c*-BN as a function of pressure at
629 room temperature in this study in comparison with that from previous studies (Datchi and
630 Canny 2004; Ono et al. 2015). The red dotted line, black dotted line, blue dotted line, and
631 green dotted line is the data fitting results of this study, Datchi and Canny 2004, One et al.
632 2015, and Sanjurjo et al. 1983, respectively. Error bars are smaller than symbols.

633 **Figure 3:** 3D-surface fitting of Raman shifts of *c*-BN as a function of temperature (K)
634 and pressure (GPa).

635 **Figure 4:** (a) Pressure difference ΔP(%) changes with increasing experimental pressure
636 (P). (b) Pressure difference ΔP(%) changes with increasing experimental temperature (T).
637 ΔP(%)=(P1-P2)/P1*100%, P1 is the pressure determined by Eq. 6, P2 is the pressure
638 determined by Eq. 7.

639 **Figure 5:** Raman shift of the TO mode of *c*-BN linearly changes with different grain
640 sizes as a function of laser power.

641 **Figure 6:** The real-time in-situ photomicrographs and the corresponding Raman spectra
642 of *c*-BN (TO mode) and quartz in DAC at 1.83 GPa and 293 K, 5.00 GPa and 573 K, 0.48
643 GPa and 873 K, 0.65 GPa and 1023 K, respectively. The pressure and temperature are
644 determined by Eq. 6 and the thermocouple, respectively.

645 **Figure 7:** The real-time in-situ photomicrographs and the corresponding fluorescent
646 spectra of Sm^{2+}:SrB_4O_7 and quartz in DAC at 1.32 GPa and 293 K, 4.58 GPa and 573 K,
647 773 K, 1023 K, respectively. The pressure and temperature are determined by Eq. 2 and
648 the thermocouple, respectively. The latter two sets of experiments could not determine
649 the pressure due to Sm^{2+}:SrB_4O_7 and quartz dissolution or reaction with water.

650 **Figure 8:** The real-time in-situ photomicrographs of ruby and quartz in DAC at 1.44 GPa
651 and 293 K, 573 K, 873 K, 1023 K, respectively, the Raman spectra of quartz at 1.44 GPa

652 and 293 K and the fluorescent spectra of ruby at1.44 GPa and 293 K, 573 K, 873 K, 1023
653 K, respectively. The experimental pressure and temperature determined by the Eq. 1 and
654 the type K thermocouple, respectively.
655
656 **Supplementary Figure Captions**
657
658 **Figure S1:** Representative fluorescence spectra (R doublet) of a ruby sphere at 1 atm and
659 different temperatures.
660 **Figure S2:** Heating stage in room-P and high-T experiment (a) The HRTS1000 heating
661 stage under the Raman system microscope. (b) Temperature calibration process using the
662 melting points of four metals (63A solder, tin, zink, and silver). (c) Temperature
663 correction curve from the reading temperature to the actual temperature.
664 **Figure S3:** High-temperature diamond anvil cell (BX-90) used for all high-P experiments.
665 (a) Photograph of the high-temperature BX-90 DAC. (b) Section view of BX90 DAC of
666 which (1) outer cylinder part, (2) inner piston part, (3) screws for generating loading force,
667 (4) pack of conical spring washers, (5) setscrews for diamond anvils alignment, (6) safety
668 setscrews, (7) optional miniature Ni-Cr resistance heater, (8) K-type thermal couple, (9)
669 rhenium gasket, and (10) diamond anvils (modified from Kantor et al. 2012). (c) Detailed
670 drawing of the sample chamber and diamond anvils: the ruby sphere, Sm^{2+}:SrB_4O_7

671 powder and *c*-BN are placed into the sample chamber of the rhenium gasket at the same
672 time and it is filled with pure helium gas as the pressure media.

673 **Figure S4:** (a) Fluorescent spectra of the 0–0 line of Sm^{2+}:SrB_4O_7 under various
674 temperatures at room pressure. (b) The fitting process of the fluorescent spectra of the 0–
675 0 line of Sm^{2+}:SrB_4O_7 at high pressure and high temperature.

676 **Figure S5:** Wavelength shift of the 0–0 line of Sm^{2+}:SrB_4O_7 as a function of temperature
677 at room pressure. Error bars smaller than symbols are not shown for clarity.

678 **Figure S6:** Pressure-temperature paths of the diamond anvil experiments for each run.

679

680 **TABLES CAPTIONS**

681 **Table 1:** High P-T induced Raman shift of *c*-BN in comparison with that from previous
682 studies.

683 **Table S1:** All results of the high-P and/or high-T experiments in this study.

Table 1. High P-T induced Raman shift of *c*-BN in comparison with that from previous studies

ν_0	T	dv/dT	d^2v/d^2T	P	dv/dP	d^2v/d^2P	$d^2v/(dP \cdot dT)$	Reference
1053.6 (2)	293-1223	-0.0221(7)	$1.100(7)\times10^{-5}$	0-46	3.35(2)	-0.011(1)	0.00105(7)	This study
1054	300-723			0-21	3.33	-0.018	0.00022	Datchi and Canny 2004
	300-1600	-0.038						Alvarenga et al. 1992
				0-8.2	3.39			Sanjurjo et al. 1983
				0-83.9	3.35	-0.013		Ono et al. 2015
	300-1840	-0.01	2.8×10^{-5}					Herchen et al. 1993

Notes: the values of ν_0 were measured at ambient pressure (1 bar) and temperature (20 °C) in cm^{-1}. T is the temperature in K; P is the pressure in GPa.

Fig. 1

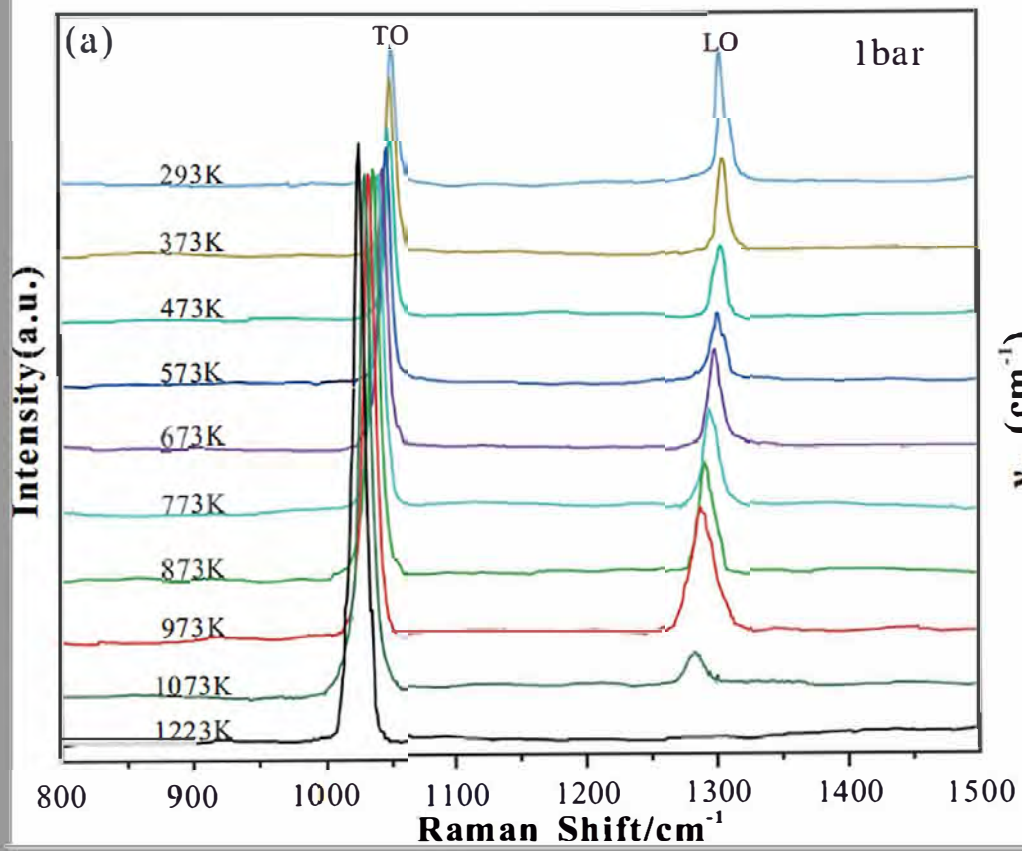
(a)
TO
LO
1bar
293K
373K
473K
573K
673K
773K
873K
973K
1073K
1223K
Intensity(a.u.)
800
900
1000
1100
1200
1300
1400
1500
Raman Shift/cm-1

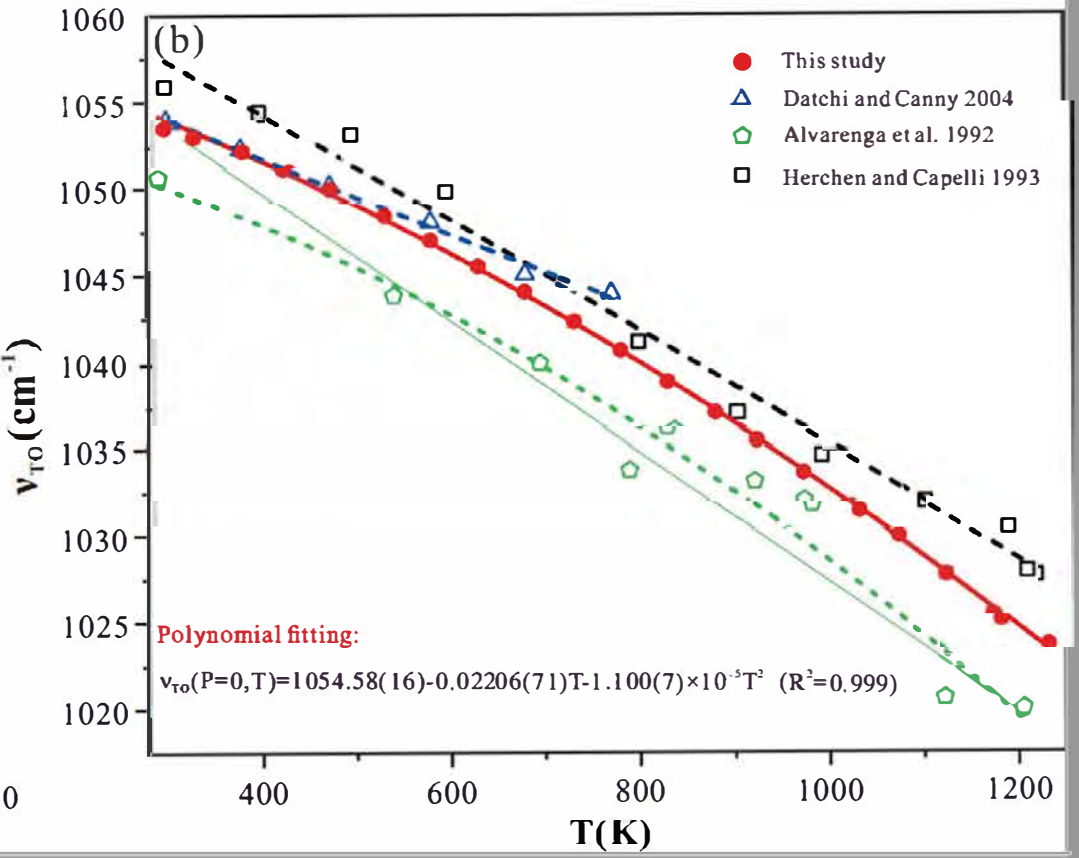
(b)
This study
Datchi and Canny 2004
Alvarenga et al. 1992
Herchen and Capelli 1993
Polynomial fitting:
νTO(P=0,T)=1054.58(16)-0.02206(71)T-1.100(7)×10-5T2 (R2=0.999)
1060
1055
1050
1045
1040
1035
1030
1025
1020
νTO(cm-1)
400
600
800
1000
1200
T(K)

Fig. 2

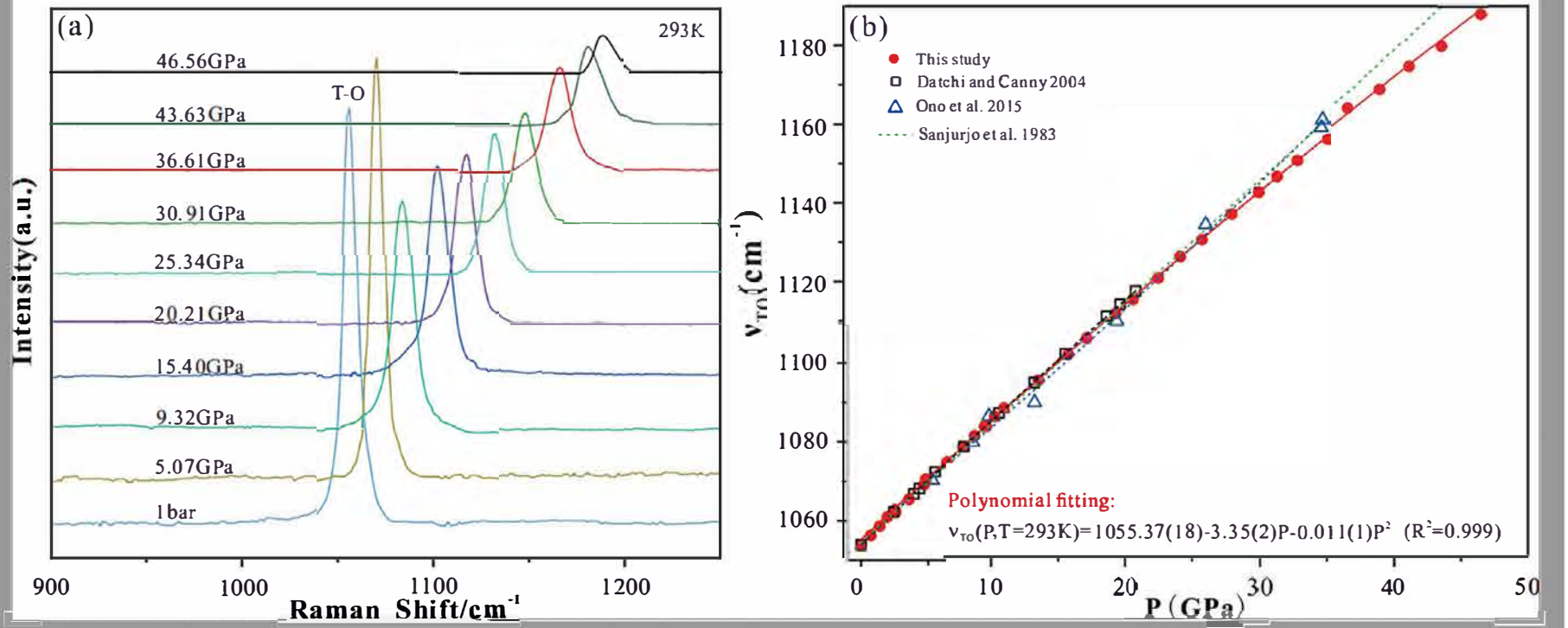
(a)
293K
46.56GPa
43.63GPa
36.61GPa
30.91GPa
25.34GPa
20.21GPa
15.40GPa
9.32GPa
5.07GPa
1bar
T-O
Intensity(a.u.)
900
1000
1100
1200
Raman Shift/cm-1
(b)
This study
Datchi and Canny 2004
Ono et al. 2015
Sanjurjo et al. 1983
Polynomial fitting:
vTO(P,T=293K)=1055.37(18)-3.35(2)P-0.011(1)P2 (R2=0.999)
vTO(cm-1)
1060
1080
1100
1120
1140
1160
1180
0
10
20
30
40
50
P (GPa)

Fig. 3

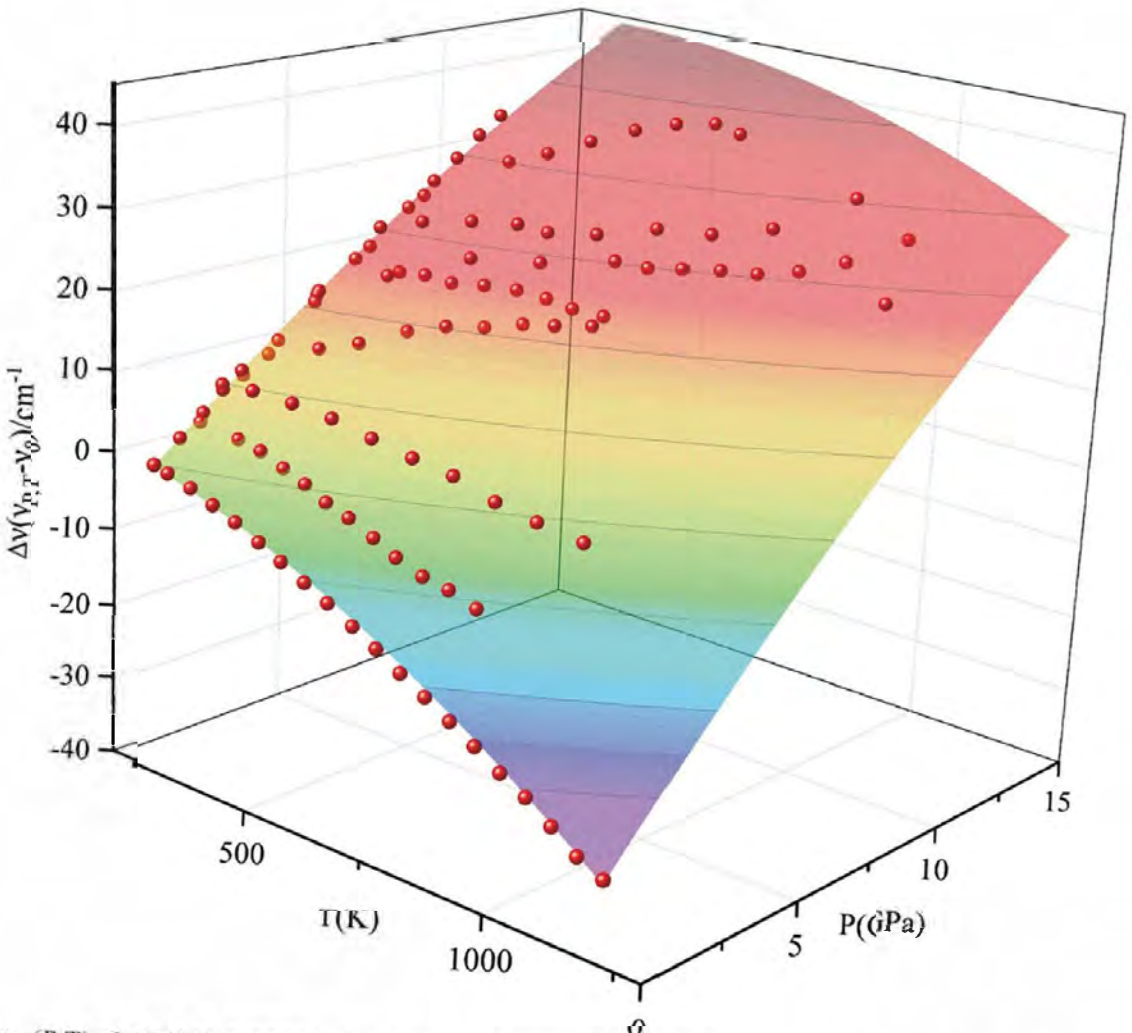

$\Delta\nu_{TO}(P,T)=2.81(51)-0.0053(16)T-1.78\times10^{-5}(11)T^2+3.47(6)P-0.055(6)P^2+0.00105(7)PT$ (R^2=0.998)

Fig. 4

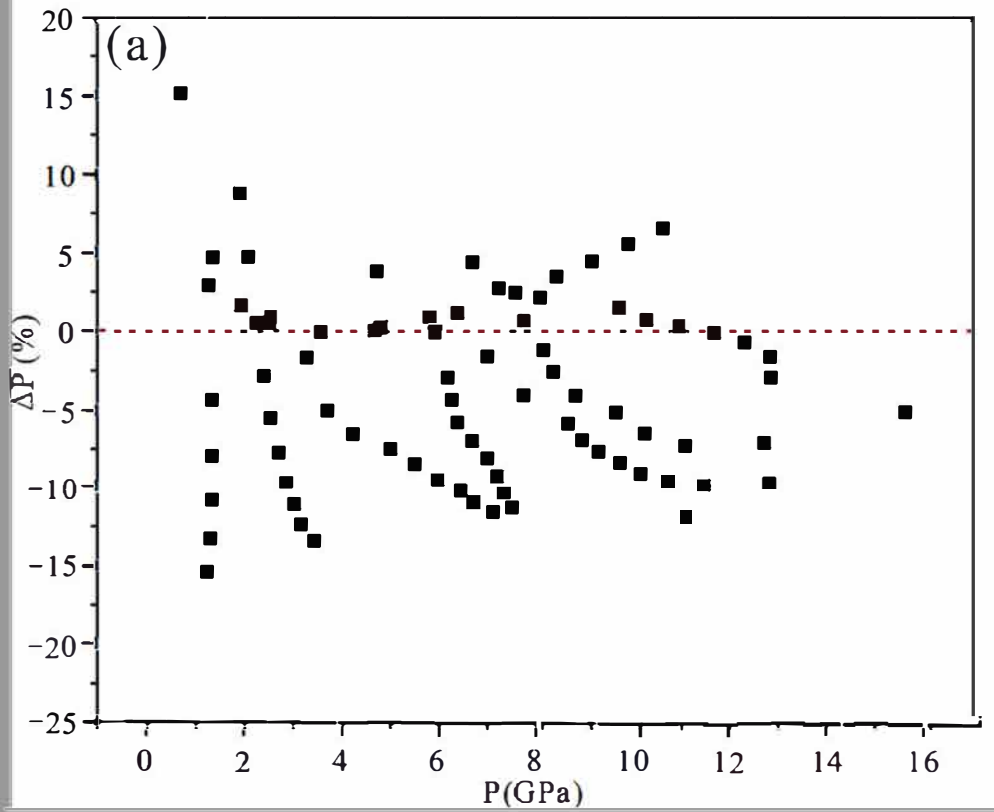
(a)
ΔP (%)
P(GPa)
20
15
10
5
0
−5
−10
−15
−20
−25
0
2
4
6
8
10
12
14
16

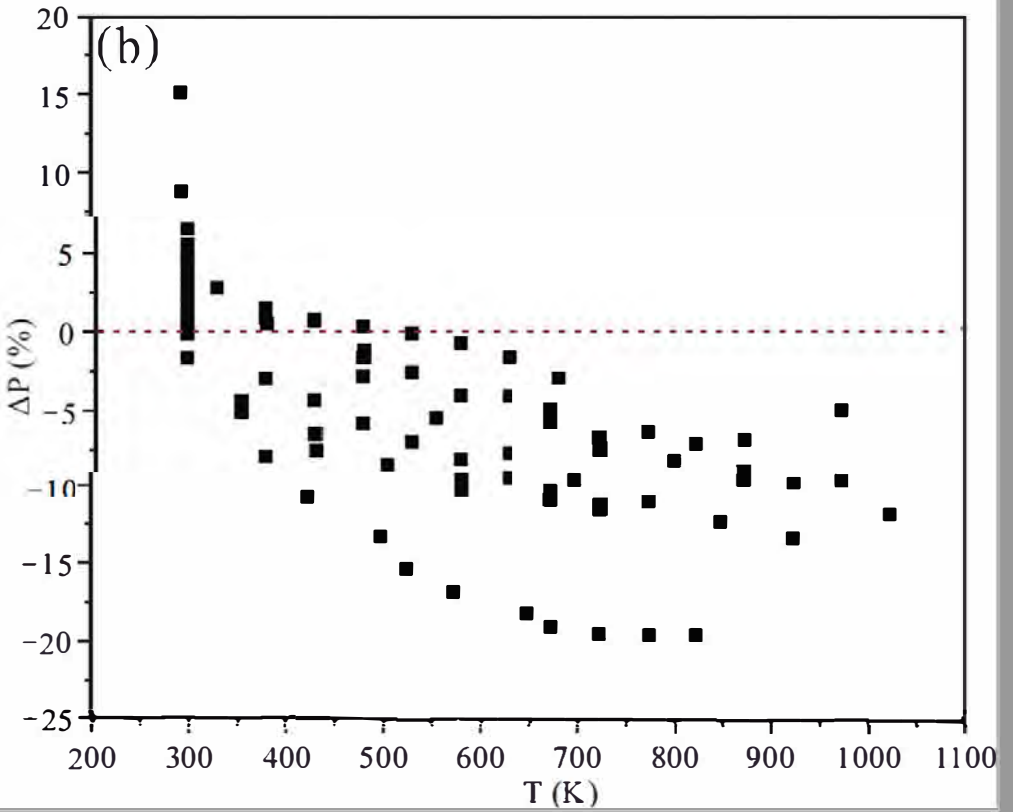
(b)
ΔP (%)
T (K)
20
15
10
5
0
−5
−10
−15
−20
−25
200
300
400
500
600
700
800
900
1000
1100

Fig. 5

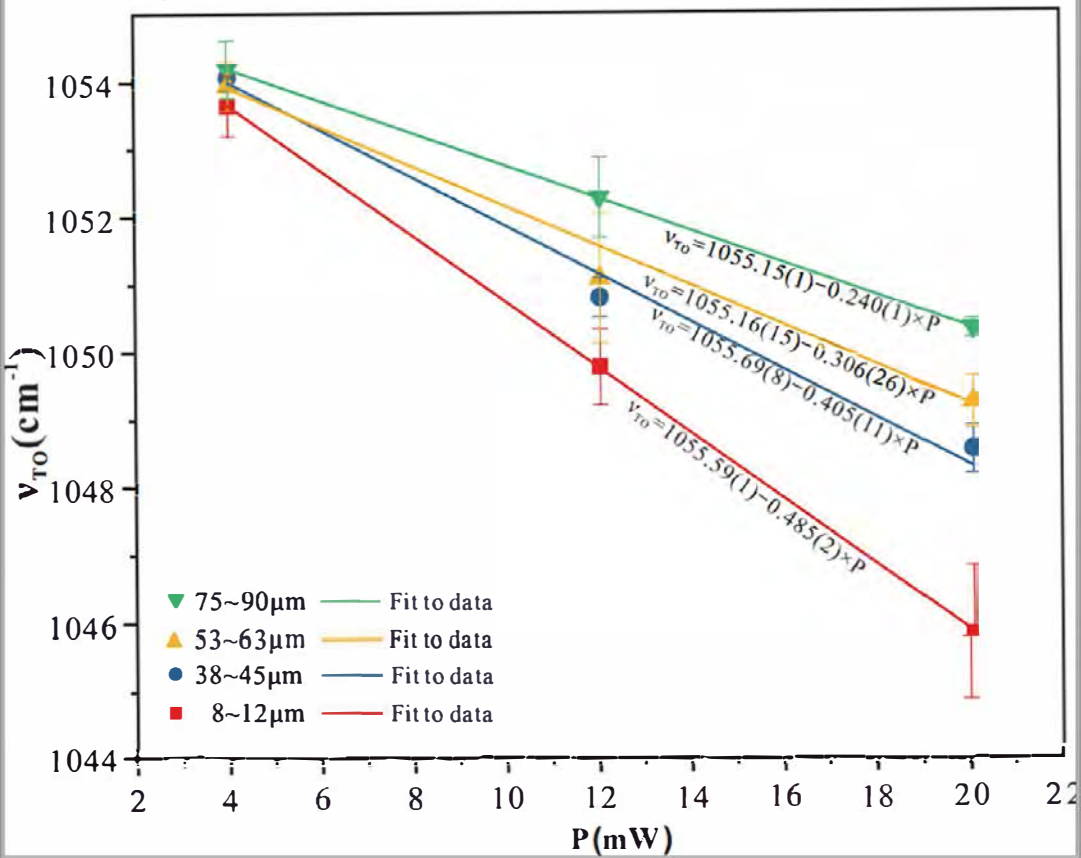
1054
1052
1050
1048
1046
1044
2
4
6
8
10
12
14
16
18
20
22
ν_{TO}(cm^{-1})
P(mW)
ν_{TO}=1055.15(1)−0.240(1)×P
ν_{TO}=1055.16(15)−0.306(26)×P
ν_{TO}=1055.69(8)−0.405(11)×P
ν_{TO}=1055.59(1)−0.485(2)×P
75~90μm
53~63μm
38~45μm
8~12μm
Fit to data
Fit to data
Fit to data
Fit to data

Fig. 6

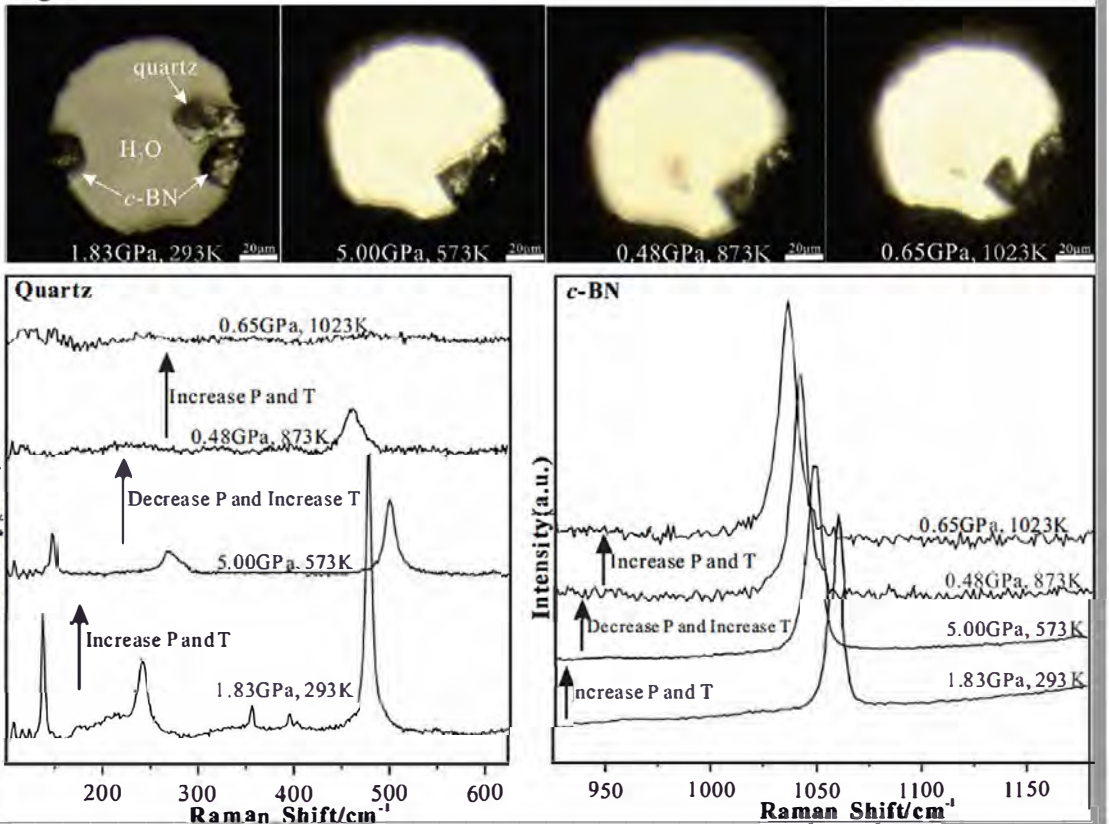
quartz
H2O
c-BN
1.83GPa, 293K
5.00GPa, 573K
0.48GPa, 873K
0.65GPa, 1023K
Quartz
0.65GPa, 1023K
Increase P and T
0.48GPa, 873K
Decrease P and Increase T
5.00GPa, 573K
Increase P and T
1.83GPa, 293K
Intensity(a.u.)
200
300
400
500
600
Raman Shift/cm-1
c-BN
0.65GPa, 1023K
Increase P and T
0.48GPa, 873K
Decrease P and Increase T
5.00GPa, 573K
Increase P and T
1.83GPa, 293K
Intensity(a.u.)
950
1000
1050
1100
1150
Raman Shift/cm-1

Fig. 7

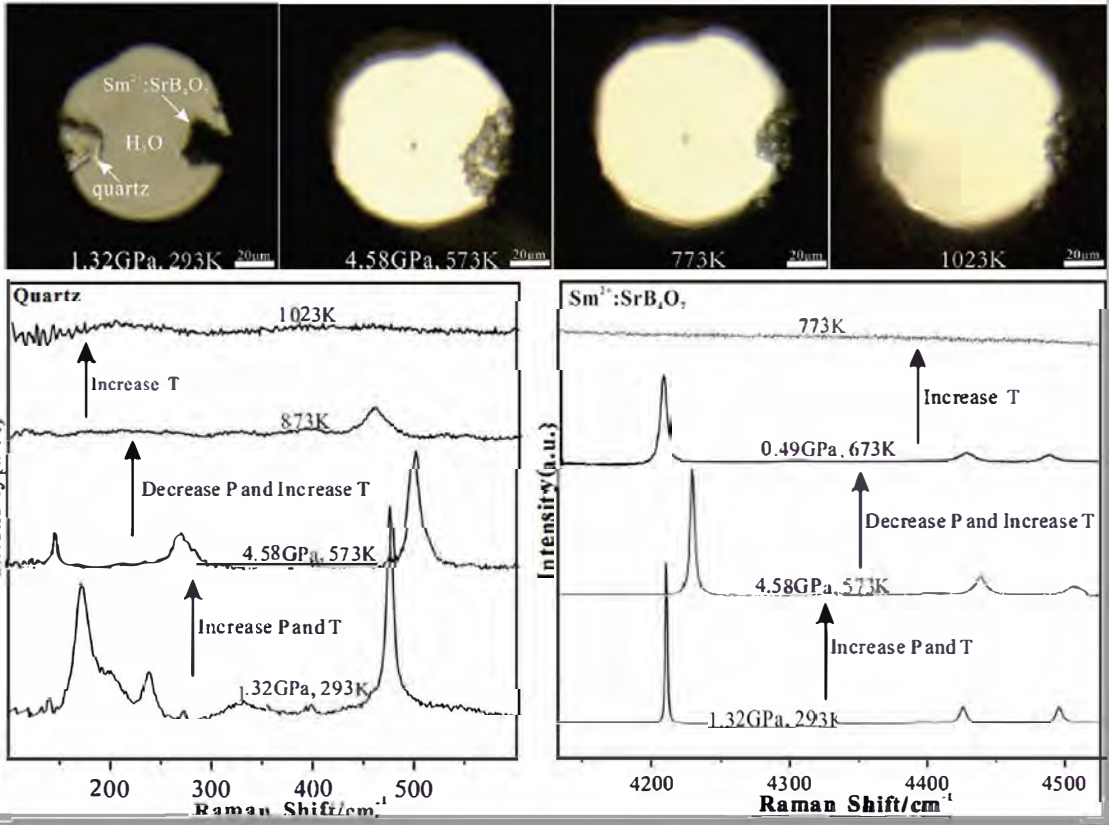
Sm3+:SrB4O7
H2O
quartz
1.32GPa, 293K
4.58GPa, 573K
773K
1023K
Quartz
1023K
Increase T
873K
Decrease P and Increase T
4.58GPa, 573K
Increase P and T
1.32GPa, 293K
Intensity(a.u.)
200
300
400
500
Raman Shift/cm-1
Sm3+:SrB4O7
773K
Increase T
0.49GPa, 673K
Decrease P and Increase T
4.58GPa, 573K
Increase P and T
1.32GPa, 293K
Intensity(a.u.)
4200
4300
4400
4500
Raman Shift/cm-1

Fig. 8

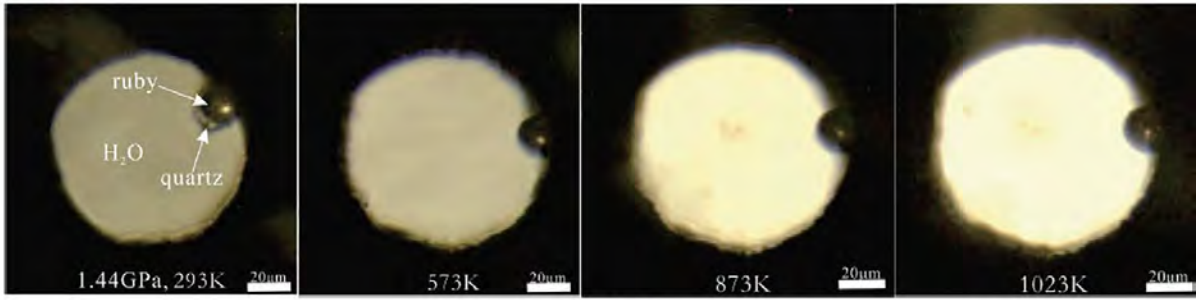
ruby
H_2O
quartz
1.44GPa, 293K
20um
573K
20um
873K
20um
1023K
20um

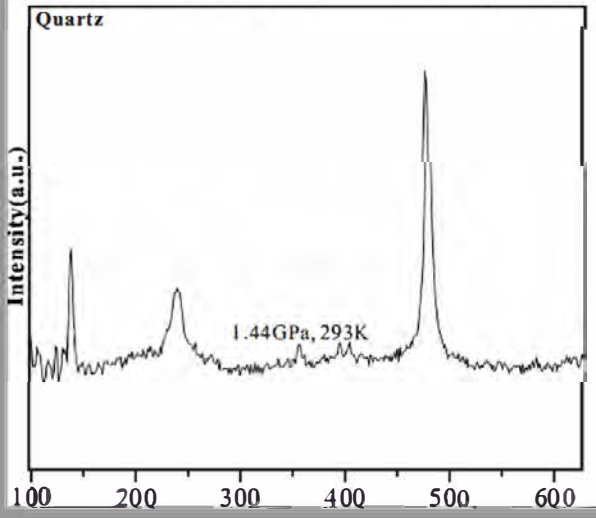
Quartz
Intensity(a.u.)
1.44GPa, 293K
100
200
300
400
500
600

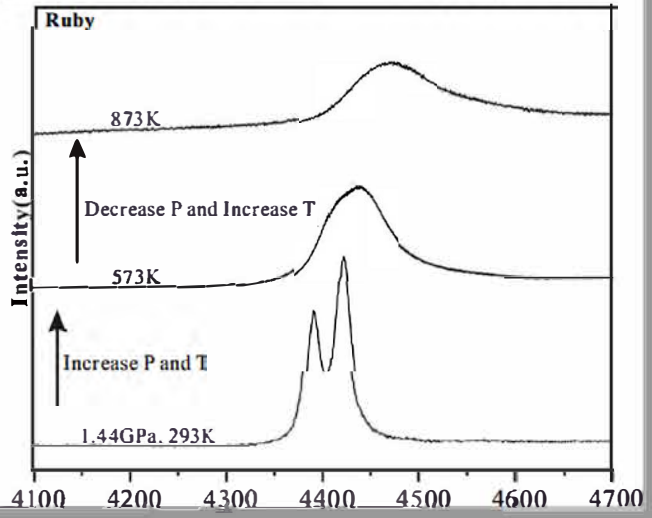
Ruby
Intensity(a.u.)
873K
Decrease P and Increase T
573K
Increase P and T
1.44GPa, 293K
4100
4200
4300
4400
4500
4600
4700